

Investigation of Control Approaches for a High Precision, Piezo-actuated Rotational Stage Operating under External Disturbances at CERN

Niklas Ericson

Master of Science Thesis in Electrical Engineering
**Investigation of Control Approaches for a High Precision, Piezo-actuated
Rotational Stage Operating under External Disturbances at CERN**

Niklas Ericson

LiTH-ISY-EX-YY/NNNN-SE

Supervisor: **Mark Butcher**
 CERN, Geneva, Switzerland
 Måns Klingspor
 ISY, Linköpings University, Sweden

Examiner: **Svante Gunnarsson**
 ISY, Linköpings University, Sweden

*Division of Automatic Control
Department of Electrical Engineering
Linköping University
SE-581 83 Linköping, Sweden*

Copyright © 2016 Niklas Ericson

Abstract

The Equipment Controls and Electronics section at CERN is developing a high precision piezo-actuated rotational stage for the UA9 crystal collimation project. Several control-related issues arising from the complexity and operational environment of the system make it difficult to design a controller that achieves the desired performance. This thesis aims to identify different control approaches that can be applicable to this rotational stage and similar high precision systems.

Contents

1	Introduction	1
1.1	Background	1
1.2	Motivation	2
1.3	Purpose and goal	2
1.4	Prospective challenges	2
1.5	Related work	3
1.6	Approach	3
1.7	Limitations	3
1.8	Outline	3
2	System overview	5
2.1	Crystal collimators	5
2.2	Rotational stage	5
2.3	Piezoelectric Stack Actuators	6
2.3.1	Hysteresis Effect	7
2.3.2	Creep Effect	7
2.4	Rotational Stage Modeling	7
2.4.1	Maxwell-slip Model	8
2.4.2	Linear System Identification	10
2.5	Present Control Approach	10
3	Theory	13
3.1	Model Reference Adaptive Control	13
3.1.1	Perturbation Estimation	14
3.1.2	Adaptive laws	14
3.2	Integral Resonance Control	15
4	Results	19
4.1	Benchmark tests	19
4.2	Linear dynamics characterization	20
4.3	Simulation Results	20
4.3.1	Model Reference Adaptive Control	20
4.3.2	Integral Resonance Control	25

5 Conclusions and Future work	35
5.1 Conclusions	35
5.2 Future work	35
Bibliography	37

1

Introduction

1.1 Background

High precision positioning systems are vital in e.g. scanning tunneling microscopes (STM), atomic force microscopes (AFM) and in semiconductor lithography. In AFM, for instance, high precision positioning is required to control the vertical position of the scanning probe to keep the force constant between the sample surface and the probe tip. An topographical image of the sample is obtained by raster-scanning the probe over the sample surface and plotting the vertical displacement against the probe's x-y position. A positioning system that keeps the force constant down to an atomic-scale resolution is thus inevitable in order to obtain a high resolution image without damaging the sample [4].

The piezoelectric effect is a phenomenon that arises in certain solid materials when an electric potential is generated in response to applied mechanical stress. The effect was first discovered by Jacques and Pierre Curie in 1880 when they found that applying pressure to a quartz crystal generates electrical potential. Today, the effect is commonly encountered in daily life and utilized in for example lighters, buzzers and loudspeakers.

Smart materials such as piezoelectric and magnetostrictive materials are nowadays commonly used in precision actuators due to their ability to convert electrical energy into mechanical energy. Piezoelectric materials have been commercially available for almost 45 years and have become indispensable for the nanopositioning industry [5]. In cases where a relatively small displacement range is required (travel ranges up to 500 μm) a piezo electric device is the actuator of choice due to its fast response, high resolution and its ability to generate large mechanical forces for small amounts of power in compact designs [4].

The ECE (Equipment Controls and Electronics) section in the Engineering Department at CERN (European Organization for Nuclear Research) is developing a

high precision positioning system for use in the UA9 crystal collimation study.

1.2 Motivation

Crystalline solids have the ability to constrain the directions that particles take as they pass through, this is commonly called the "channeling" property. The UA9 collaboration at CERN is investigating how tiny bent crystals can help to steer particle beams in modern hadron colliders such as the Large Hadron Collider (LHC) [12]. In high energy colliders particles tends to drift outwards creating a beam halo. These particles surrounding the beam, can be lost and cause damage to sensitive parts in the accelerator, such as the superconducting magnets which can suffer an abrupt loss in superconducting capability (quench), even from a small dose of deposited energy. To extract and absorb these halo particles, CERN uses a multi-stage collimation system, consisting of primary and secondary collimators connected in series. CERN's largest particle accelerator, the LHC operating at 7 TeV, has 108 collimators distributed along 2 beam pipes [9]. At the moment, these collimators use massive blocks of amorphous material to intercept and absorb halo particles. The UA9 experiment aims to develop a new collimator, utilizing the technique of a bent crystal and a single absorber which will, in theory, imply in a more efficient cleaning, a less complex system and a reduction of the machine impedance. These are all essential for reaching higher energy levels in a future particle accelerator.

1.3 Purpose and goal

One major difficulty that arises with the use of bent crystals is that, the higher the energy of the particle, the lower the angular acceptance for channeling. Hence, a high precision rotational mechanism is required. For this purpose, the ECE section is developing a rotational stage that will rotate the crystal with a high angular accuracy. This purpose of this thesis is to identify possible control approaches that could be applicable to the rotational stage in order to achieve the desired performance. The stage is required to:

- have a total range of 20 mrad.
- be able to track reference trajectories at ramp rates of 100 μ rad/s.
- reject external disturbances to maintain a maximum tracking error of $\pm 1 \mu$ rad even when the linear axis is moving.

1.4 Prospective challenges

First of all, piezoelectric actuators show strong nonlinear properties such as hysteresis and creep (drift), which have to be compensated for. Moreover, the mechanical flexural structure in combination with the piezo electric characteristics

leads to a highly resonant structure, making it difficult to achieve the desired performance while operating the rotational stage within noisy environments with external disturbances such as ground vibrations. Furthermore this rotational stage is attached to a linear stage which is composed by a leadscrew, a stepping motor and an axis. The linear movement adds additional perturbation to the rotational stage due to imperfections in the leadscrew and detent torque and stepping nature of the motor. Finally the system dynamics also show linear position dependence requiring a controller that is robust to such variations.

Moving center of rotation, Disturbad yaw, pitch and roll during linear movement. 2 main drawbacks limiting accuracy and speed of nanopositioning stages. Inherent hysteresis nonlinearity in the piezoceramic material and low damped resonant modes due to the mechanical dynmaics.

1.5 Related work

One attempt to achieve the desired performance has already been made. The proposed controller, presented in [3] delivers reasonable performance but does not fulfill the requirements during movement. The authors proposes a PID controller in combination with a pre-filter, and a hysteresis compensator. The controller has shown high disturbance rejection at the first resonance peak as well as good tracking performance.

1.6 Approach

- What are the possible control approaches that can be used to achieve the desired performance?
- Which one is the most promising approach with respect to simulated/benchmarked results and ease of implementation on the real device?

1.7 Limitations

This thesis will solely focus on the control approaches

1.8 Outline

This thesis plan presents an overview of the thesis, including method, literature base and expected results. The method and work flow of the thesis as well as a comprehensive literature review is given in Chapter ???. In Chapter 4 the results that can be expected half way through the project is discussed while a brief summary of the thesis can be found in Chapter 5.

2

System overview

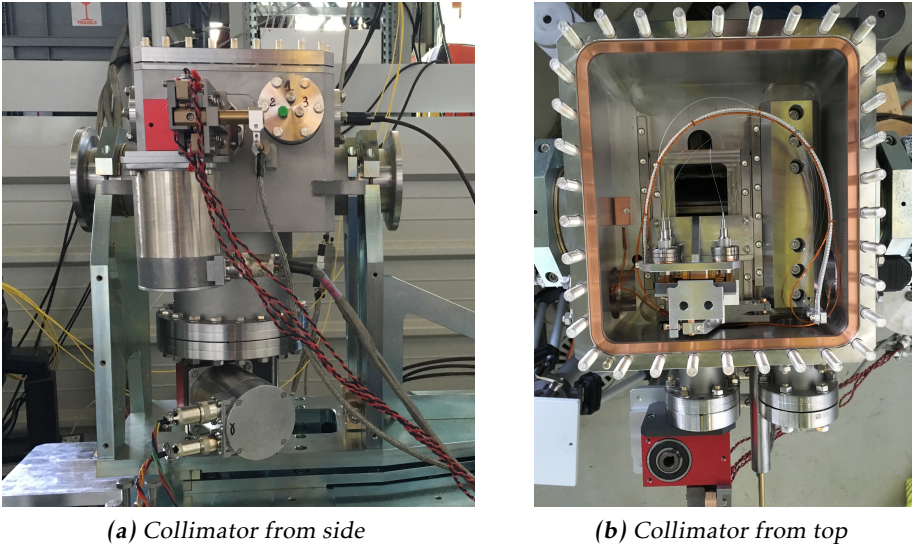
This chapter provides the reader with a brief overview of the whole collimator system used in the LHC at CERN as well as a more detailed description of the rotational stage, which is the device in focus in this thesis.

2.1 Crystal collimators

A collimator is a specially designed device, built to interfere with the beam and clean it from surrounding halo particles. To be able to meet the future demand of higher energy levels, a more efficient collimator is being developed at CERN. This new collimator will utilize a crystalline solid to extract particles from the beam. The collimator consists of a T-shape structure containing two movable linear axes and one rotational stage. Each linear axis is driven by a stepping motor, labeled as $M1$ and $M2$ in Figure 2.1a, separately controlled in open-loop by an individual drive unit. The motor driving the vertical axis, $M1$, is used to move a piece of beampipe down inside the T-shape, giving access to the horizontal axis, driven by $M2$, to move the rotational stage (including the crystal) into the beampipe to interfere with the beam. The directions of the crystal's linear and rotational movement are indicated by the arrows in Figure 2.1b. During operation, Physicists will drive the crystal close to the beam, enter it with an angle and rotate it slightly (in the range of 10 mrad) until the channeling effect is detected. Channeled particles will then be bent off the beam core and absorbed further down the beam pipe.

2.2 Rotational stage

The rotational stage as shown in Figure? is composed by a monolithic structure, a prestressed piezo stack actuator and an interferometer measurement system.



(a) Collimator from side

(b) Collimator from top

Figure 2.1: Illustrates the collimator from the side (a) and the top (b).

The flexure-hinge based structure, avoids sliding parts and thereby enhance precision by reducing the number of nonlinear effects (e.g. backlash and friction). A prestressed piezo stack actuator is exploited to generate the rotaional movement by interacting on a point 4mm away from the center of rotation, see Figure. This amplifying structure gives the rotational stage a range of 20 mrad. For the measurement system, 3 interferometric heads are placed as in Figure ?, pointing towards a mirror mounted ontop of to the rotaional head, perpendicular to the plane of rotation. The setup allows for measurements of both the yaw and roll angle (the coordinate system is defined with respect to the beam). The yaw angle is used as feedback to the rotational stage control loop. The spring, depicted in Figure?, prestresses the PEA in order to enhace the overall stiffness of the stage as well as keeping the stackplates in place (the stack is nonglued to be sufficient in a radioactive area). This combinataion leads to an unmistakable resonant structure, due to the characteristics of the PEA demanding in combination with the spring, demanding a properly designed controller. The system moving the crystal, i.e. the linear axis driven by M_2 and the rotaional stage needs to be able to track reference trajectories at ramp rates of 100 $\mu\text{rad/s}$ and reject external disturbances to maintain a maximum tracking error of $\pm 1 \mu\text{rad}$.

2.3 Piezoelectric Stack Actuators

The rotational stage uses a linear piezoelectric stack actuator to create the movement. It provides a displacement range from 0 to 30 μm , corresponding to 0 and 150V, respectively. The actuators are made of many thin, stacked electroactive

ceramic disks, electrically connected in parallel. This construction allows for an actuator that can exhibit the highest stiffness of all actuators designs but still with a high displacement range [5].

2.3.1 Hysteresis Effect

The hysteresis effect is a nonlinear effect that is present during the operation of piezoelectric actuators. It occurs when the driving direction is reversed and originates from the polarization and the molecular effects in the piezoceramic. It depends on the amplitude of the applied voltage but also on the frequency of input signals [10]. Figure 2.2 illustrates the hysteresis effect. One can see how the same voltage value, e.g. 60V corresponds to an angular position of 5,2 μrad in one direction and to 7,2 μrad in the opposite direction.

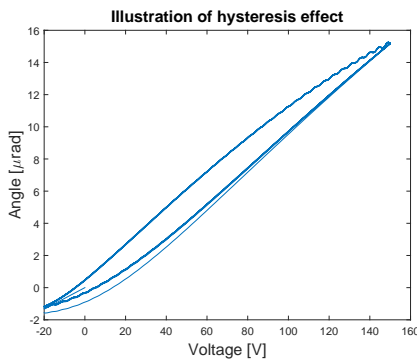


Figure 2.2: Illustration of the hysteresis effect.

2.3.2 Creep Effect

The creep effect is another nonlinear effect that is present during the operation of piezoelectric actuators. The effect is a slow elongation or contraction of the actuator displacement over time, with a constant driving signal and is caused by thermal effects in the piezoceramics. Figure 2.3 illustrates the creep effect. One can see how the rotational stage slightly drifts in rotation after the applied negative step.

The creep effect is in this project (and many others) efficiently suppressed by the feedback controller requiring no precise modeling and cancellation techniques.

2.4 Rotational Stage Modeling

The piezoactuated rotational stage is modelled by a Hammerstein structure, adopted by the authors in [3], allowing them in principal, to decouple the nonlinear hysteresis from the linear system dynamics. The employed Hammerstein structure

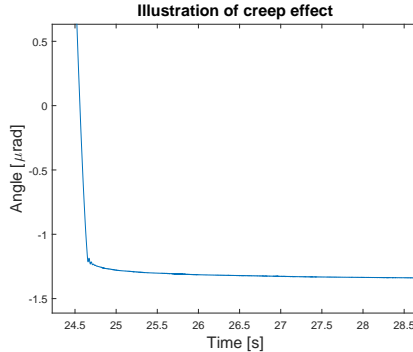


Figure 2.3: Illustration of the creep effect. Note that the creep effect can last up to 10-15 minutes even if the plot only shows the development over 4 seconds.

is depicted in Figure 2.4 and consists of a *Static Hysteresis* (rate independent) model and a *Linear Dynamics* model. PEAs are known to show hysteretic behavior with a nonlocal memory (the current output does not only depend on the current input voltage but also on its history) as described in [2]. This behaviour is modeled by a generalised Maxwell-slip compensation model, described in 2.4.1. The extracted linear dynamics is identified using the described procedure in 2.4.2

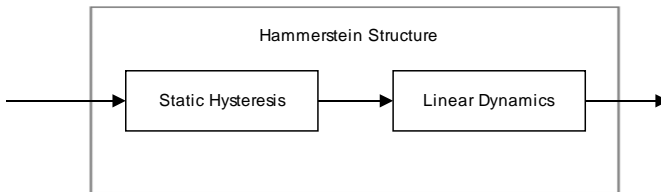


Figure 2.4: Block diagram of the Hammerstein structure, consisting of two blocks in series, modeling the static hysteresis and the linear dynamics, respectively.

2.4.1 Maxwell-slip Model

A generalized Maxwell-slip is used to model the hysteresis effect. It uses a parallel n^{th} order elasto-slide element system with a friction force acting on each element, to create a nonlinear model. An elasto-slide element consist of a massless spring connected in series with a massless block that is subject to Coulomb friction. The model is summarized in the following equations and described more thoroughly in [11].

$$F_i = \begin{cases} k_i(x - x_{bi}) & \text{if } k_i|x - x_{bi}| < f_i \\ f_i \operatorname{sgn}(\dot{x}) \text{ and } x_{bi} = x - \frac{f_i}{k_i} \operatorname{sgn}(\dot{x}) & \text{else} \end{cases} \quad (2.1)$$

$$F = \sum_{i=1}^n F_i \quad (2.2)$$

Where F_i is (in terms of the rotational stage) the applied voltage, x the rotational displacement, x_b blocked displacement and k_i, f_i are unkown parameters where $i = 1 \dots n$. The model parameters have been estimated by fitting the model to the major hysteresis loop, obtained by acquiring data from the system with a 0.5 Hz input driving signal as described in [2, 3]. The result is presented in Figure 2.5 and Table 2.1 where $n = 10$.

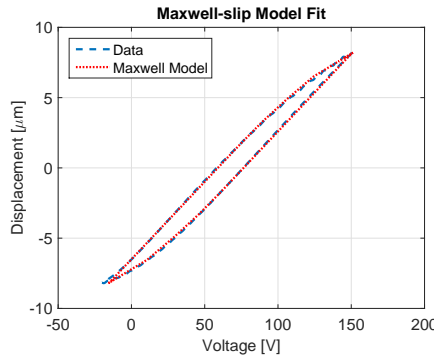


Figure 2.5: The plot shows the model fit of the Maxwell slip model to the acquired hysteresis of the rotational stage. The fit has a mean squared error of 1.1464.

i	k_i	f_i
1	4.53	3.69
2	0.90	1.46
3	1.01	2.47
4	0.36	1.16
5	1.49×10^{-6}	4.28×10^{-6}
6	2.89×10^{-7}	1.41×10^{-6}
7	1.59×10^{-7}	9.10×10^{-7}
8	1.39×10^{-7}	9.10×10^{-7}
9	2.28×10^{-7}	1.67×10^{-6}
10	4.58	37.30

Table 2.1: Identified parameters of the Maxwell slip model.

2.4.2 Linear System Identification

The extracted linear dynamics has been identified as an 6th order Output-Error system using a PRBS as excitation signal, allowing for a valid extraction from the nonlinear dynamics. The system transfer function has been derived in discrete-time using the the System Identification Toolbox in Matlab. A more detail description of the procedure is available in [3]. Figure 2.6 shows a comparison between the model and the real system in the frequency domain, where the Fast Fourier Transform (FFT) identification is calculated by dividing the FFT of the output with the FFT of the input.

The transfer function of the model, discretized with a sampling time of 0.5 ms, is presented in (2.3).

$$G_o(z) = \frac{21.05z^{-1} - 6.85z^{-2} + 8.52z^{-3} - 0.71z^{-4} + 9.30z^{-5}}{1 - 1.85z^{-1} + 1.09z^{-2} + 0.016z^{-3} - 1.32z^{-4} + 1.55z^{-5} - 0.48z^{-6}} \quad (2.3)$$

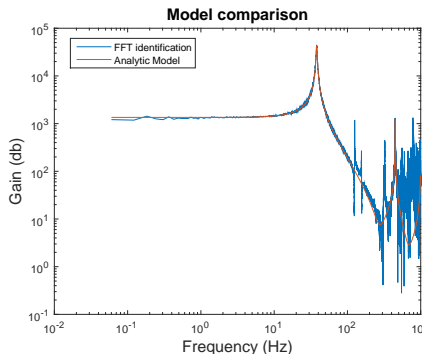


Figure 2.6: The plot shows the model fit of the Maxwell slip model to the acquired hysteresis of the rotational stage. The fit has a mean squared error of 1.1464.

2.5 Present Control Approach

The original controller for the rotational stage is a 2-DOF structure (feedback and pre-filter). A schematic overview of the control loop is depicted in Figure 2.7, consisting of a controller block C, a prefilter F, a disturbance d and the linearized rotational stage $G = G_o H^{-1}$, where G_o , H^{-1} is the linear dynamics and the hysteresis compensator, respectively.

The controller block (C) is a series combination of a PID controller, notch filter and a lead network, aiming to stabilize the system (PID), increase the sufficient phase margin (lead) and make the system robust to high frequency oscillations (notch). Since the bandwidth of the system is relatively low, $f_b = 58\text{Hz}$ according to Figure 2.6, it has been decided to exclude cancellation of the first resonance

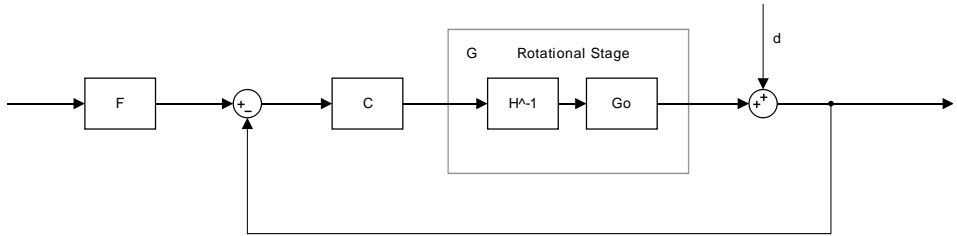


Figure 2.7: Block diagram of the present control loop, including controller, prefilter and hysteresis compensator.

peak in order to keep the bandwidth as high as possible and have a sufficient attenuation on the sensitivity function [3]. The PID controller, lead network and notch filter are all presented below in (2.4).

$$F = \frac{0.0029z - 0.0029}{z^3 - 2.91z^2 + 2.816z - 0.91} \quad (2.4a)$$

$$C_{PID} = \frac{0.47z^2 - 0.94z + 0.47}{z^2 - 1.78z + 0.78} \quad (2.4b)$$

$$C_{lead} = \frac{4.20z^2 - 7.72z + 3.55}{z^2 - 1.67z + 0.69} \quad (2.4c)$$

$$C_{notch} = \frac{0.28z^4 - 0.62z^3 + 0.75z^2 - 0.59z + 0.26}{z^4 - 1.95z^3 + 1.39z^2 - 0.40z + 0.039} \quad (2.4d)$$

3

Theory

This chapter presents the motivation and the theory behind each of the control approaches investigated in this thesis.

3.1 Model Reference Adaptive Control

An adaptive controller has the ability to adjust the system response by updating the parameters of a feedback controller in real time, resulting in a controller that is less sensitive to changes in the model and aging of the system. One approach is to use a reference model to create the desired system response which the adaptive laws will aim for, this approach is known as the Model Reference Adaptive Controller (MRAC). This model does not require any prior knowledge about the model uncertainties, implying in a more straight forward way to implement precision control to nanopositioning systems. Moreover, this scheme allows for the use of a lower order model (in relation to the system model) since the online parameter estimation can be used sufficiently with a lower order model. The MRAC scheme can be extended to include perturbation estimation (MRACPE), giving the controller the ability to compensate for various unmodelled effects, including both linear and nonlinear perturbations. Nonlinear effect such as the hysteresis are treated as lumped perturbations to the nominal system model and can be compensated for in the same manner as linear, using the knowledge of the system and the previous measurement and output signal. The MRACPE also allows the maximum tracking error to be predefined.

3.1.1 Perturbation Estimation

Using a second order model, the adaptive laws can be derived as follows. Consider the system model stated below.

$$\ddot{x}(t) + \alpha_1 \dot{x}(t) + \alpha_0 x(t) = \beta_0 u(t) + f(t) \quad (3.1)$$

where $x(t)$ denotes the output rotation at time t , $u(t)$ the input voltage at time t and $\alpha_1, \alpha_0, \beta_0 \in \mathbb{R}$ are known system constants. $f(t)$ is a function describing the unknown perturbations of the system, including the hysteresis and creep effect. The general equations for deriving the perturbation function are described more thoroughly in [6], for a simple second order SISO model the perturbation estimation is derived to

$$\hat{f}(t) = \ddot{x}_{cal}(t) + \alpha_1 \dot{x}_{cal}(t) + \alpha_0 x(t) - \beta_0 u(t - T_s) \quad (3.2)$$

where $x_{cal}^{(n)}$ denotes the calculated state, T_s is the sampling time interval and $u(t - T_s)$ is the control input in the previous timestep. $u(t - T_s)$ is often approximated to $u(t)$ in practice which is valid approximation if T_s is sufficiently small. Denote that $x(t)$ here is the sensor input, i.e. the measured yaw angle.

Each state is, for its computational efficiency, computed by a simple backward different equation depicted below.

$$x_{cal}^{(n)}(t) = \frac{x_{cal}^{(n-1)}(t) - x_{cal}^{(n-1)}(t - T_s)}{T_s} \quad (3.3)$$

3.1.2 Adaptive laws

The objective of the adaptive laws is to calculate the control parameter so that they converges to ideal values resulting in a system response that matches the reference. The adaptive laws can be derived using Lyapunov theory which is outlined in this section. Consider the second order reference model below

$$\ddot{x}_m(t) + a_1 \dot{x}_m(t) + a_0 x_m(t) = b_0 u_d(t) \quad (3.4)$$

where $x_m(t)$ denotes the output rotation, $u(t)$ the input voltage and a_0, a_1, b_0 are known positive constants.

The tracking error is defined as below.

$$e(t) = x(t) - x_m(t) \quad (3.5)$$

Recalling (3.1), replacing $f(t)$ with the estimation $\hat{f}(t)$ and subtracting it from (3.7) gives the following expression, more details can be found in [10].

$$\ddot{e}(t) + a_1 \dot{e}(t) + a_0 e(t) = (a_1 - \alpha_1) \dot{x}(t) + (a_0 - \alpha_0) x(t) - b_0 u_d(t) - \beta_0 u(t) + \hat{f}(t) \quad (3.6)$$

Transforming it into state-space form

$$\dot{\mathbf{E}} = \mathbf{A}\mathbf{E} + \beta_0 \mathbf{B}u + \Delta \quad (3.7)$$

where

$$\mathbf{E} = \begin{bmatrix} e \\ \dot{e} \end{bmatrix}, \mathbf{A} = \begin{bmatrix} 0 & 1 \\ -a_0 & -a_1 \end{bmatrix}, \mathbf{B} = \begin{bmatrix} 0 \\ 1 \end{bmatrix}, \Delta = \begin{bmatrix} 0 \\ \delta \end{bmatrix} \quad (3.8)$$

with $\delta = (a_1 - \alpha_1)\dot{x}(t) + (a_0 - \alpha_0)x(t) - b_0 u_d(t) + \hat{f}(t)$.

If all the eigenvalues of \mathbf{A} have negative real parts, then \mathbf{E} will tend to zero as $t \rightarrow \infty$, i.e. the system is asymptotically stable. Moreover, according to Lyapunov theory [7], for each positive-semidefinite matrix \mathbf{Q} , there exist one positive-semidefinite matrix \mathbf{P} which solves (3.9).

$$\mathbf{A}^T \mathbf{P} + \mathbf{P} \mathbf{A} = -\mathbf{Q} \quad (3.9)$$

With the auxillary item $\hat{e} = \mathbf{E}^T \mathbf{P} \mathbf{B}$, the adaptive laws is given by

$$u = k_0 u_d + k_1 x + k_2 \dot{x} + k_3 \hat{f} \quad (3.10)$$

where the control law parameters is calculated as

$$\dot{k}_0 = -\eta_0 \hat{e} u_d \quad (3.11)$$

$$\dot{k}_1 = -\eta_1 \hat{e} x \quad (3.12)$$

$$\dot{k}_2 = -\eta_2 \hat{e} \dot{x} \quad (3.13)$$

$$\dot{k}_3 = -\eta_3 \hat{e} \hat{f} \quad (3.14)$$

the proof is provided in [10]. Substituting \hat{f} in (3.2) with the one in (3.10) and rearranging the parameters results in the final MRACPE control law, stated below.

$$u(t) = k_0 u_d(t) + (k_1 + k_3 \alpha_0)x(t) + (k_2 + k_3 \alpha_1)\dot{x}(t) + k_3 \ddot{x}(t) - k_3 \beta_0 u(t - T_s) \quad (3.15)$$

A block diagram of the final controller, with inspiration from Figure 9.1 in [10], is depicted in Figure 3.1. The adaptive controller consists of 4 blocks. One reference model that calcultats the desired states $Xm = [\dot{x}_m, x_m]^T$ from the input signal according to (3.7), one adaptive mechanism that implements (3.11)-(3.14) and calculates $K = [k_1, k_2, k_3, k_4]^T$, one state calculator that uses (3.3) to calculate $X = [\dot{x}, \dot{x}, x]^T$ and finaly one controller block that uses (3.15) to calcuate the control signal u that is sent to the rotaional stage.

3.2 Integral Resonance Control

The integral resonace control (IRC) can be efficiently used to damp out the first resonant mode of the system, allowing for larger controller gains and a higher control bandwidth. The IRC scheme is illustrated in Figure 3.2 and consist of a constant artificial feed-through term $D_f < 0$ and an integral controller $C = \frac{k}{s}$. The negative feed-forward term will, if sufficiently large and negative, introduce a pair of complex zeros below the first resonance frequency and ensure zero-pole

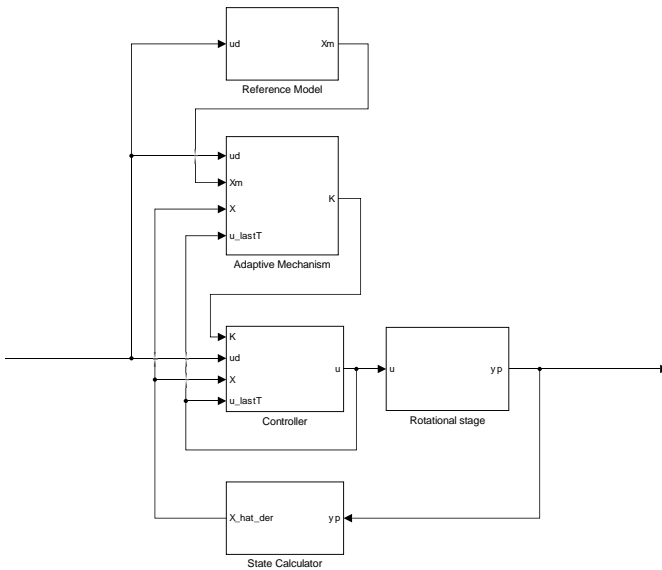


Figure 3.1: Block diagram of the adaptive controller

cancellation for higher resonance modes as shown in [1]. For stability, the phase response of the loop-gain CG_d must be within $\pm 180^\circ$ while the gain is greater than 0. The negative sign in G_d subtracts a phase of -180° . Using this knowledge, the phase margin can be easily increased by applying a simple negative integral controller to provide a 90 degrees phase lead. This results in a phase margin between $\pm 90^\circ$ which gives the system highly desired properties such as a 90° phase margin and an infinite gain margin.

The negative gain D_f is straight forward to manually select for introducing a complex pair of zeros below the first resonance. The integral gain k can be chosen by using the root locus technique and select a gain that maximizes damping.

The IRC scheme in Figure 3.2 can be simplified, by combining C and D_f in the same block, the resulting scheme is shown in the inner loop in Figure 3.3, where

$$C_2 = \frac{C}{1 + CD_f} \quad (3.16)$$

For tracking reference trajectories, the IRC can be enclosed in an outer loop, also seen in Figure 3.3, utilizing a second controller C_1 to compensate for disturbances and model errors. For the outer controller C_1 , a PI controller is sufficient but must include a negative gain to compensate for the inversion that is caused by D_f [8].

Proof for the zero-pole interlacement and the insertion of the complex con-

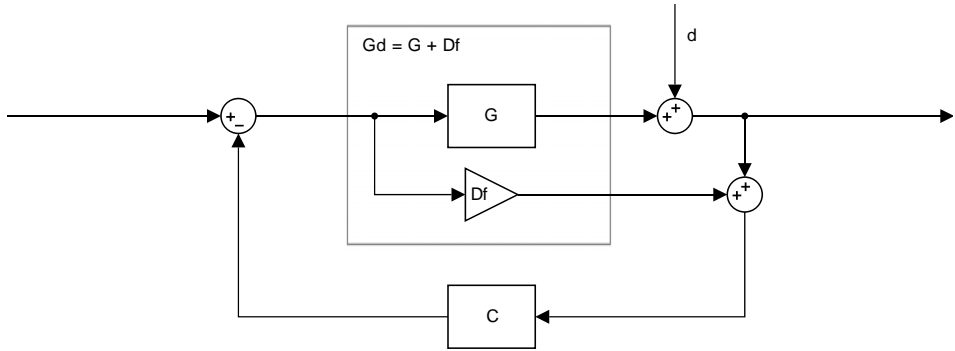


Figure 3.2: Block diagram of IRC damping loop

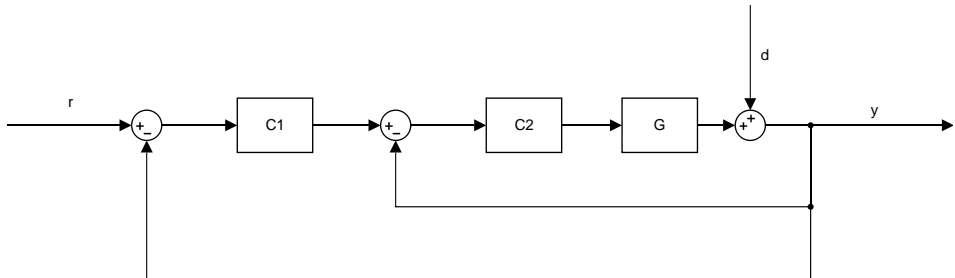


Figure 3.3: Block diagram of the tracking control system with IRC included

jugate zeros can be found in [1], but note that the proof is only given for causal systems with a relative degree of two i.e two more poles than zeros. To give the reader further information about the IRC and for a system with a relative degree of one, a brief example of a low order system is provided below.

Let G be represented as a transfer function with a relative degree of one, with 2 poles and 1 zero as written below,

$$G = \frac{s + \alpha_0}{s^2 + \beta_1 s + \beta_0} \quad (3.17)$$

where $\alpha_i > 0$ and $\beta_i > 0$, i.e. a stable and minimum phase system. Using $G_d = G + D_f$ (3.17) and rearranging the terms gives

$$\begin{aligned}
 G_d &= \frac{s + \alpha_0}{s^2 + \beta_1 s + \beta_0} + D_f \\
 &= \frac{D_f s^2 + (1 + D_f \beta_1)s + \alpha_0 + D_f \beta_0}{s^2 + \beta_1 s + \beta_0} \\
 &= \frac{D_f(s^2 + (\frac{1}{D_f} + \beta_1)s + \frac{\alpha_0}{D_f} + \beta_0)}{s^2 + \beta_1 s + \beta_0}
 \end{aligned} \tag{3.18}$$

which illustrates that the number of introduced zeros is equal to the relative degree of the transfer function and that the zeros (s_i^z) will have a negative real part if the following conditions are fulfilled.

$$Re(s_i^z) < 0 \quad \text{if} \quad \begin{cases} D_f < -\frac{1}{\beta_1} \\ D_f < -\frac{\alpha_0}{\beta_0} \end{cases} \tag{3.19}$$

4

Results

This section describes the results considering performance, robustness and stability with respect to the different control approaches. All approaches will first be benchmarked with the present control approach and presented individually in the following subsections. A comparison between all approaches is presented in the end of this chapter.

4.1 Benchmark tests

Each of the control approaches have been evaluated with respect to robustness to model errors, disturbance rejection, closed loop bandwidth and response to step, ramp and sinusoidal input, all summarized below. The prospective challenges, described in 1.4 shall be kept in mind while reading the results. Since the required ramp rates are relatively low, the disturbance rejection and the robustness to model errors are more of interest when evaluating each method.

- **Step, ramp and periodical tracking** - A step, ramp and periodic input is applied on the input to benchmark the tracking capability of the controller.
- **Disturbance rejection** - Modified step responses with impulses added to the input and measurement signal to benchmark how sensitive the system is to system disturbances.
- **Robustness to model errors** - During operation with a periodic input signal, the dynamical model is changed and the output is studied to characterize the robustness to model errors. This test is of importance since this is exactly what happens when the linear stage moves the rotational stage further out.

4.2 Simulation Results

For the comparison with the present control approach, all evaluated controllers were discretized with a sampling frequency of 2kHz. A normalized version of the high order system in (2.3) was used to model the rotational stage linear dynamics. The nonlinear dynamics, creep and hysteresis, were neglected in the simulations, assuming perfect inverse hysteresis cancellation and a sufficient closed loop to compensate for the creep effect. All simulations were performed in Matlab and Simulink.

4.2.1 Model Reference Adaptive Control

Even though the rotational stage has been modeled by (2.3), a second order model approximating the higher order system was used in the adaptive control laws to keep the computational burden low. The discretized reference model can be seen in (4.1) and all parameters and tuning variables is summarized in Table 4.1. The controller is tuned to be robust to input disturbances and model changes. The set of parameter presented in Table 4.1 is not an optimal set but a decent set of parameters that maintains stability for step sizes below 20mrad.

$$G_m(z) = \frac{7.9z + 6.7}{1313z^2 - 2095z + 796.4} \quad (4.1)$$

Parameter	Value
T_s	5×10^{-4}
α_0	5.7×10^4
α_1	7.2
β_0	7.5×10^7
a_0	5.7×10^4
a_1	1×10^3
b_0	7.5×10^7
η_0	3×10^{-2}
η_1	1×10^{-1}
η_2	1×10^{-10}
η_3	1×10^{-17}
ϵ	1×10^{-8}
Q	$diag(1 \times 10^{10}, 1 \times 10^{-3})$

Table 4.1: Parameters of the system model and the tuned adaptive controller.

Figure 4.1 shows the step response to different step sizes. Here it is clear that the system becomes unstable if the step size ≥ 26 mrad. The controller has been tuned to handle the maximum step size, i.e the rotational range of 20 mrad, which results in a longer rise time for the smaller step sizes. Note that the responses are produced with initial values $k_i = 0$, if the initial values would be set

to the values that k_i settles to, a faster step response could be expected. This can be seen in Figure 4.3 where the controller performs better for the second period.

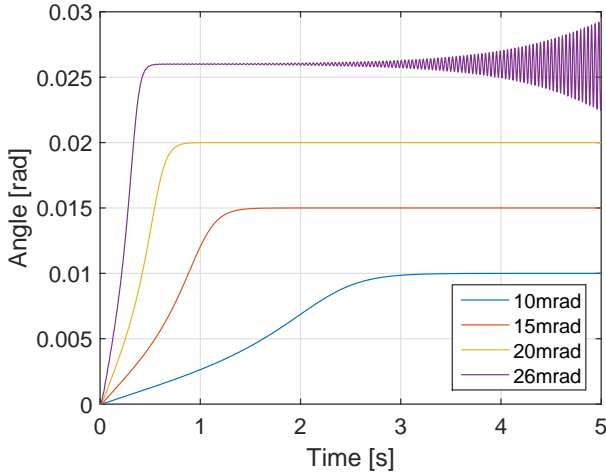


Figure 4.1: Step responses to step sizes of 10, 15, 20 and 26 mrad.

The adaptation process of the control parameters k_i , for a step response resulting from a 20mrad step, can be seen in Figure 4.2. All of the coefficients have converged within 1 second.

To illustrate the adaptation process better, a periodic response is depicted in Figure 4.3, here it is clear that after the adaptation process is finished the controller performs better for the second and third period. One can see that the adaptation process is slower for the periodic response corresponding to the amplitude of 10 mrad, hence the lower the step, the longer the adaptation time. The present controller performs well for all amplitudes.

The tracking error corresponding to the *Adaptive 20mrad* and *Present 20mrad* in Figure 4.3 can be seen in Figure 4.4. The adaptive controller performs better than the present controller after the adaptation process has finished.

A periodic response with model parameter drift is presented in Figure 4.5. It shows how the adaptive controller manages to adapt to the change in the system dynamics, while the present controller fails to do so, resulting in an unstable system. The change of the model was performed over 2 seconds, resulting in a movement of the first resonance peak, from 38 Hz to 66 Hz in frequency and from 30.1 dB to 23.5 dB in magnitude. Note that the change of the model is relatively big and for a smaller movement of the resonance peak, the present controller could still be sufficient as illustrated in Figure 4.6.

In the case in Figure 4.6 the resonance peak is only moved to 45.5 Hz and the present controller is sufficient to suppresses the disturbance. It even does it more efficiently than the adaptive controller.

Figure 4.7 and 4.8 shows the disturbance rejection capability to a disturbance on the input and output, receptively. In Figure 4.7 a small impulse was added

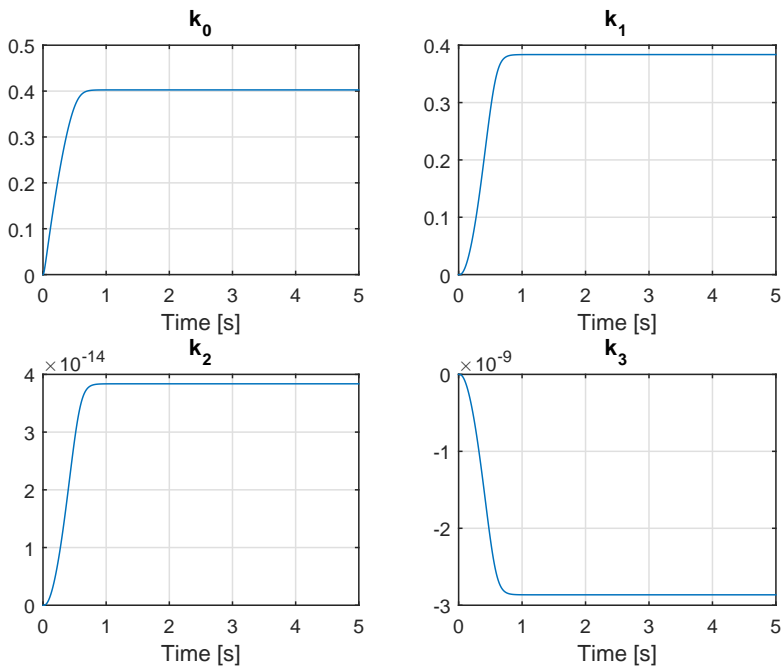


Figure 4.2: Adaptation process of control parameters k_i with a 20 mrad step.

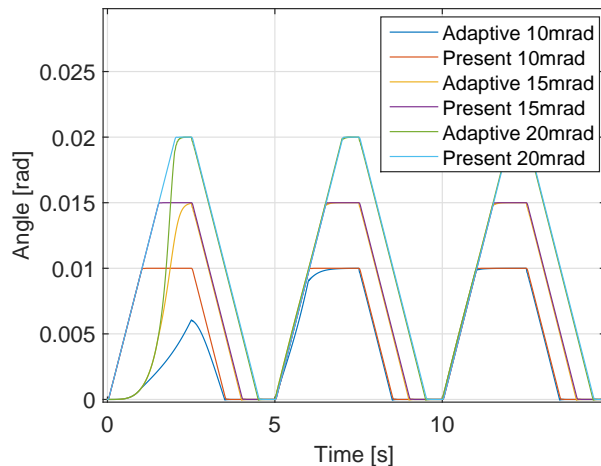


Figure 4.3: Periodic responses for the adaptive and present controller with amplitudes of 10, 15, 20 mrad.

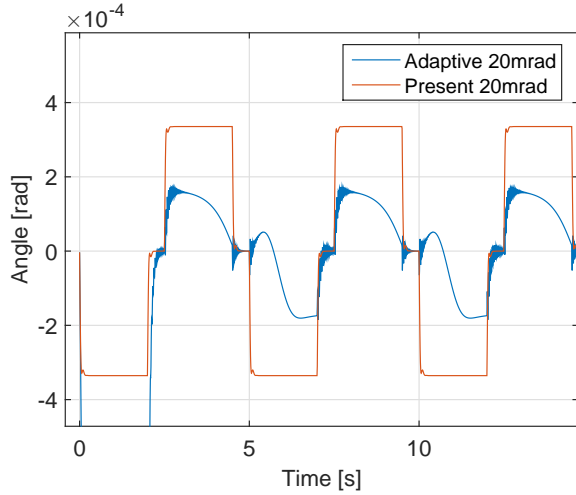
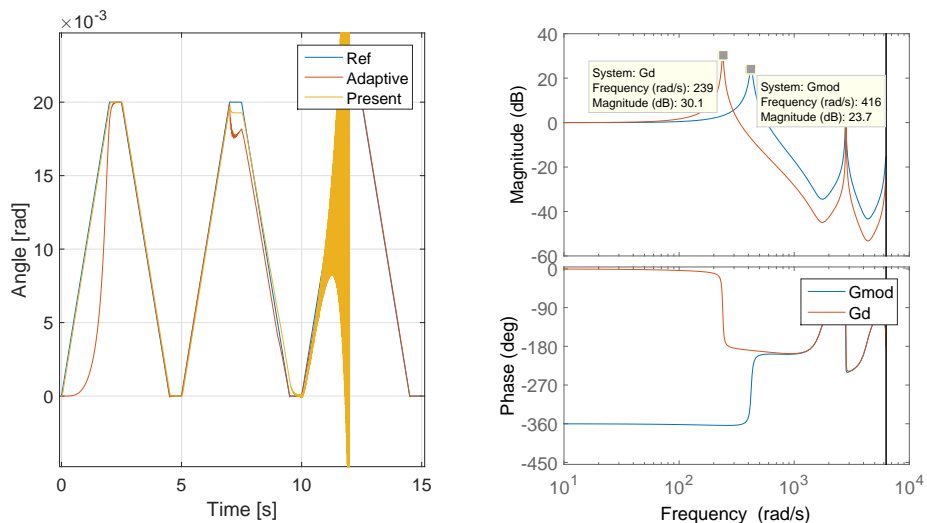


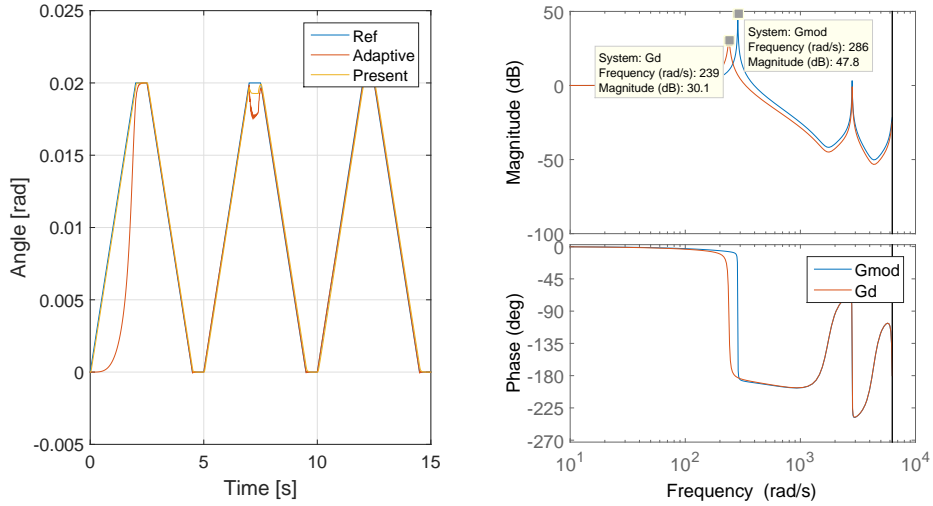
Figure 4.4: Tracking error (difference between reference and output) for the periodic response from an input signal with an amplitude of 20 mrad.



(a) Periodic response with model parameter drift.

(b) Original model (G) and the resulting model after drift (G_{mod}).

Figure 4.5: Shows the robustness to model changes over time. The model error is increased linearly from $t = 7\text{s}$ to $t = 9\text{s}$. The resulting responses is shown in (a) with the model change in (b).



(a) Periodic response with model parameter drift.

(b) Original model (G) and the resulting model after drift (G_{mod}).

Figure 4.6: Shows the robustness to model changes over time. The model error is increased linearly from $t = 7\text{s}$ to $t = 9\text{s}$. The resulting responses is shown in (a) with the model change in (b).

to the input to see if the controllers would attenuate it sufficiently. The adaptive controller performed worse than the present controller both with and without pre-filter. The present controller managed to attenuated the highest peak of the impulse by 1.5 times more than the adaptive. The settling time was also approximately 3 times worse for the adaptive controllers. In Figure 4.8 the impulse was instead added to the measured signal. Even in this case the present controller was superior, attenuating the highest peak of the impulse by 3 times more than the adaptive controller.

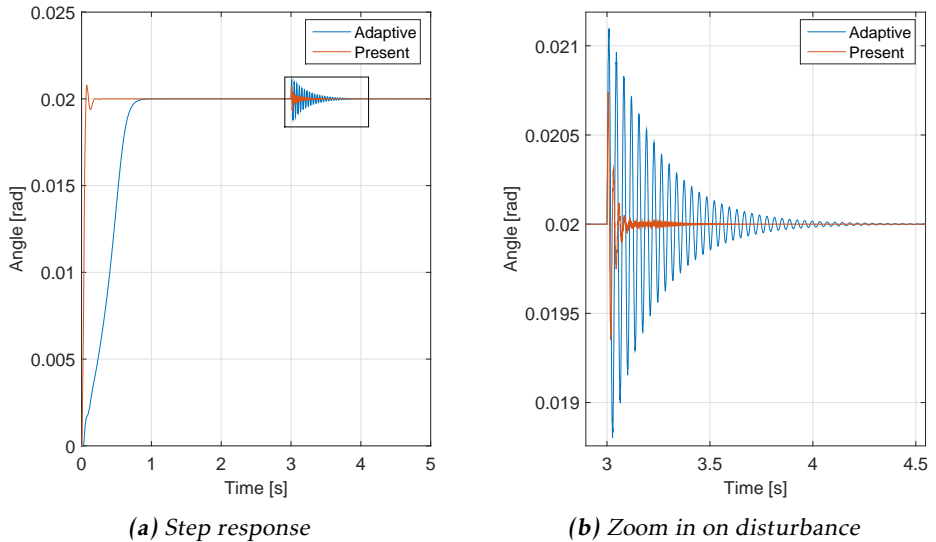


Figure 4.7: Shows how well the controller attenuates a disturbance impulse (amplitude of 5.1×10^{-3}) added to the input signal at $t = 3\text{s}$. The whole step response is shown in (a) with a zoom in on the disturbance in (b).

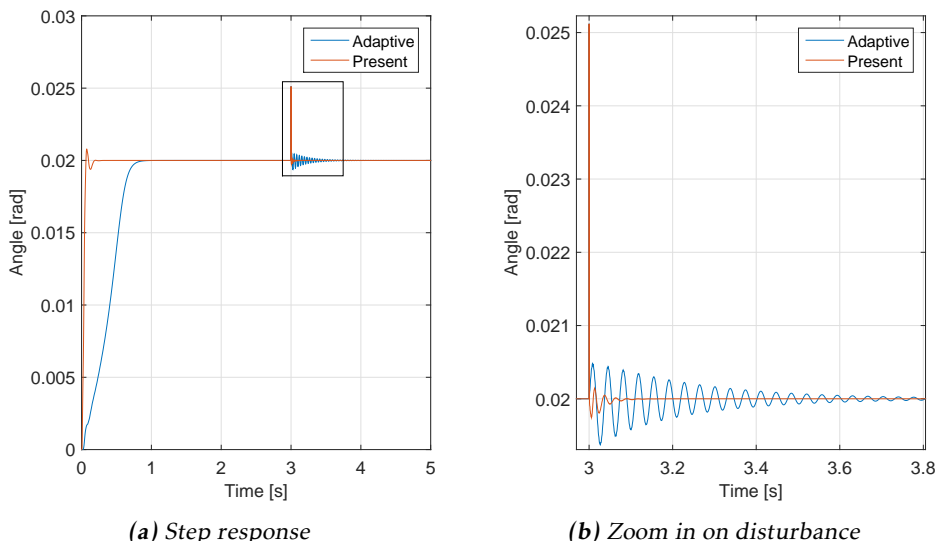


Figure 4.8: Disturbance rejection to impulses (amplitude of 5.1×10^{-3}) added to the measured signal at $t = 3\text{s}$. The step response is shown in (a) with a zoom in on the disturbance in (b).

4.2.2 Integral Resonance Control

The IRC design procedure presented in 3.2 was carried out in continuous time, but each block in the scheme was individually discretized for the sake of comparison with the present controller. The continuous time system of (2.3) consists of a system with 7 poles and 6 zeros. A negative feedforward would therefore introduce another zero and depending on the gain placing the zeros in a desired position. As seen in the pole-zero plot comparison in Figure 4.9, a feedforward of $D_f = -1.2$ was sufficient to introduce one zero and place it and its complex conjugate below the first resonance frequency. This and the zero-pole interlacing for the higher order modes can be seen in Figure 4.9b, where the zoom-in shows the complex conjugate zeros below the first resonance mode.

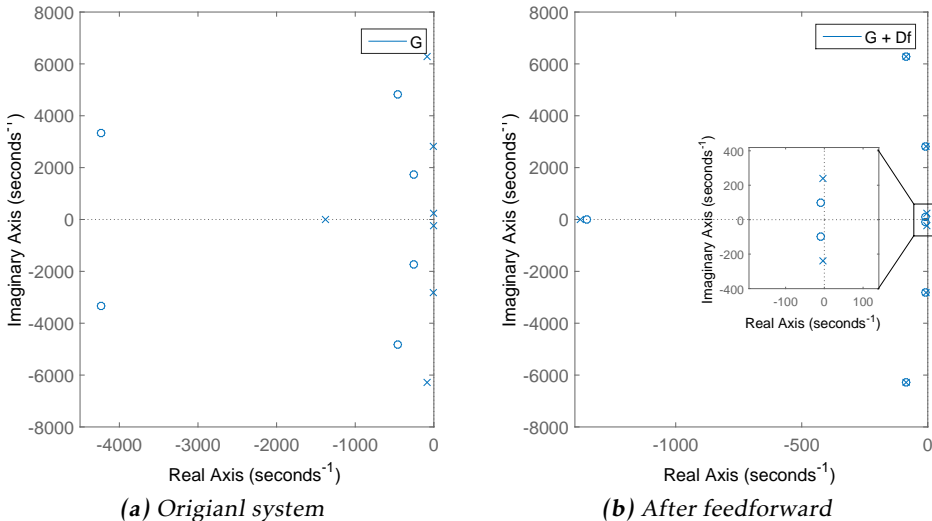


Figure 4.9: Comparison of pole-zero plot before and after adding the negative feedforward. After adding the feedforward to the system which poles and zeros are shown in (a), the zeros and poles are interlacing as seen in (b).

The corresponding bode plot can be seen in Figure 4.10, showing the complex conjugate pair of zeros as a dip before the first resonance peak.

The integral controller $C = \frac{-k}{s}$ was added according to Section 3.2 and a gain of $k = 314$ was found to maximize the damping, by using the root locus technique. The open and closed loop system of the IRC damping loop depicted in Figure 3.2 is shown in Figure 4.11. It is clear that the integral controller damps out the first resonance peak efficiently in closed loop.

Finally, the damped system was enclosed in an outer loop with a second controller C_1 for reference tracking capability. C_1 was designed to be robust to model errors i.e. keep the sensitivity function G_{dy} , stated in (4.2), low for the frequen-

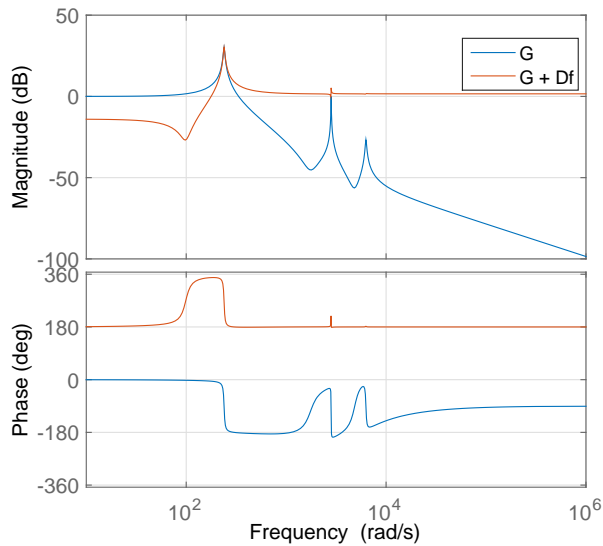


Figure 4.10: Bode plot of the system before and after the addition of the negative feedforward.

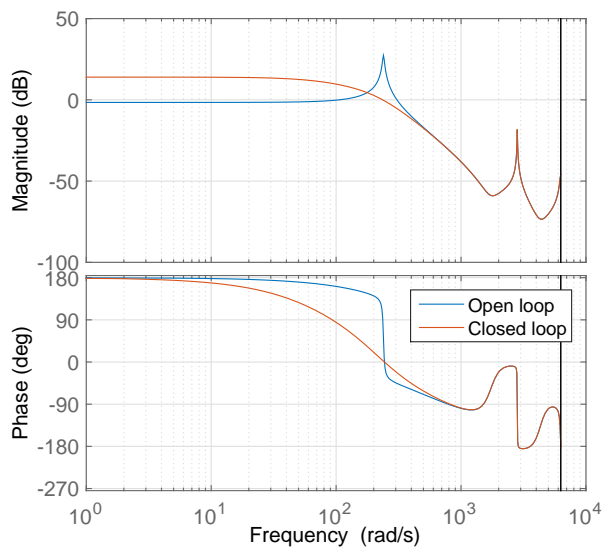


Figure 4.11: Open and closed loop of the IRC damping loop.

cies that the model changes with, (d and y in G_{dy} can be found in the block scheme in Figure 3.3). C_1 was designed in Matlab's SISO-Tool and is presented in (4.3).

$$G_{yd} = \frac{1}{1 + C_2 G(1 + C_1)} \quad (4.2)$$

$$C_1 = \frac{-13.54z^5 + 40.92z^4 - 57.47z^3 + 55.89z^2 - 35.87z + 10.05}{z^5 - 1.65z^4 + 0.80z^3 - 0.16z^2 + 0.014z - 0.00042} \quad (4.3)$$

The resulting closed loop system and the sensitivity function is shown in Figure 4.12 and 4.13, respectively. The plots show that the use of the IRC has increased the closed loop bandwidth from 11 Hz to 73 Hz, corresponding to an increase of 6.5 times the present closed loop bandwidth.

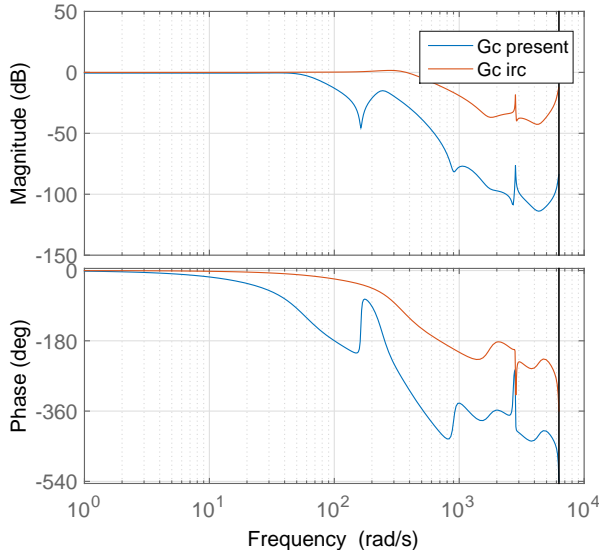


Figure 4.12: Closed loop system of the IRC and the present approach

The IRC sensitivity function also shows that the IRC scheme attenuates model disturbances better in the low frequency range and in the region within 24-64 Hz.

The IRC tracking performance is shown in Figure 4.14. One can conclude that the IRC approach is able to eliminate the constant ramp tracking error which the present doesn't handle, see Figure 4.14a. Hence the tracking error in Figure 4.14 is a lot lower for the IRC approach.

The robustness test performed for the adaptive controller was done for the IRC controller accordingly. Figure 4.15a shows the response to minor model changes

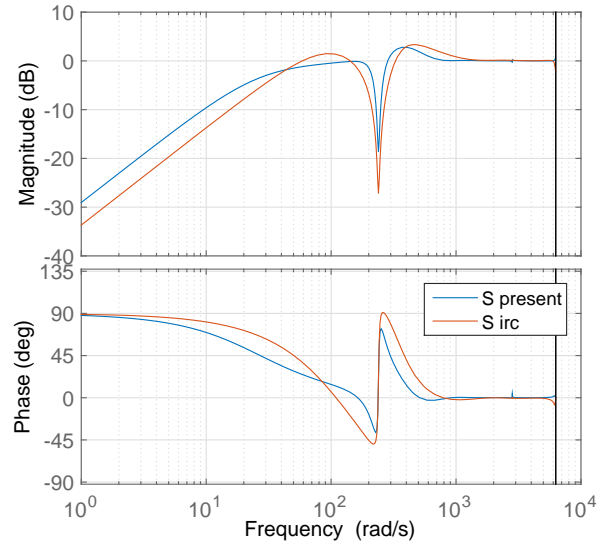


Figure 4.13: Sensitivity function (G_{dy}) of the IRC and the present approach

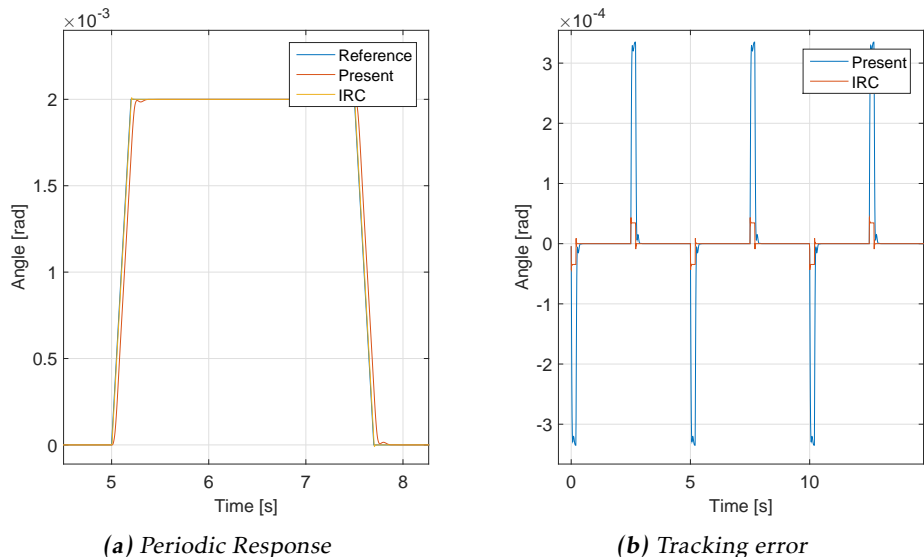


Figure 4.14: Periodic response of the IRC and the present controller. A zoom in on one period is shown in (a) while the tracking error over three periods are shown in (b).

depicted in Figure 4.6b. While Figure 4.15b shows the response corresponding to a larger drift in the model according to Figure 4.5. The IRC handles the model drift better than the present controller in both cases, even when the model change is major and the system with the present controller becomes unstable.

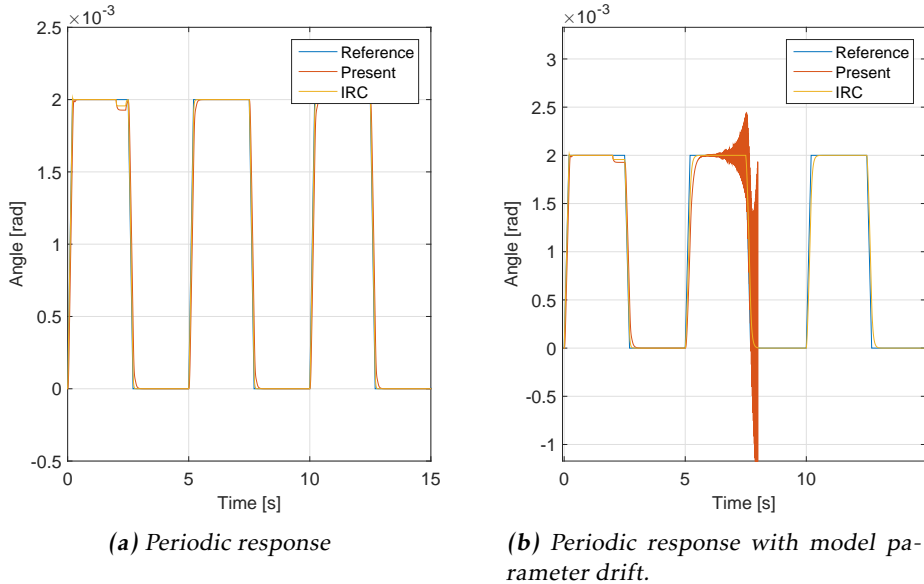


Figure 4.15: Shows the robustness to model changes over time. The model error is increased linearly from $t = 3\text{s}$ to $t = 5\text{s}$. The resulting responses are shown in (a) while the model change is presented in (b).

The IRC capability of rejecting disturbances on the input signal is shown in Figure 4.16.

The IRC capability of rejecting disturbances on the output signal is shown in Figure 4.17. Since the impulse is added directly on the output the steps response peaks accordingly at $t = 3\text{s}$. It is hard to tell from Figure 4.17b, but the peak is visible for both of the control approaches. After the peak, the methods perform similarly, with a slightly higher damping and amplitude for the IRC oscillations shown in the zoom in. To further verify the controller capability of handling disturbances with various frequencies, a white noise was added to the d signal shown in Figure 3.3. The FFT was then taken on the output to verify that the result was similar to the obtained sensitivity function in Figure 4.13. The FFT result is shown in Figure 4.18 and indeed shows a similar result.

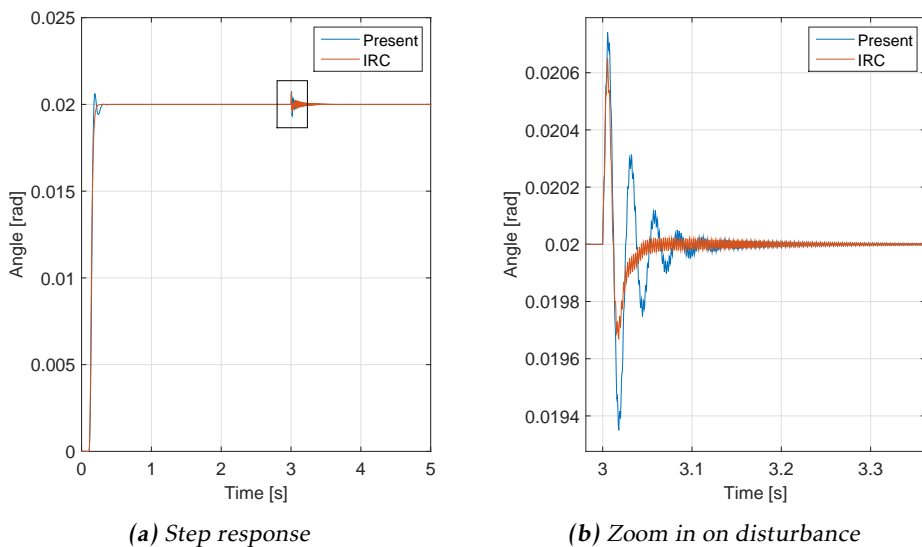


Figure 4.16: Shows how well the controller attenuates a disturbance impulse (amplitude of 5.1×10^{-3}) added to the input signal at $t = 3\text{s}$. The whole step response is shown in (a) while a zoom in on the disturbance is presented in (b).

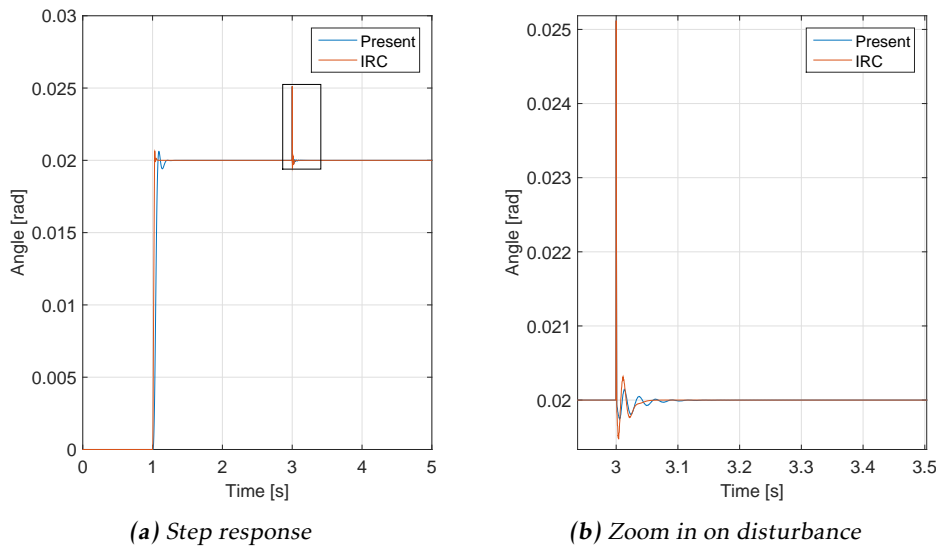


Figure 4.17: Shows how well the controller attenuates a disturbance impulse (amplitude of 5.1×10^{-3}) added to the measured signal at $t = 3\text{s}$. The whole step response is shown in (a) while a zoom in on the disturbance in (b).

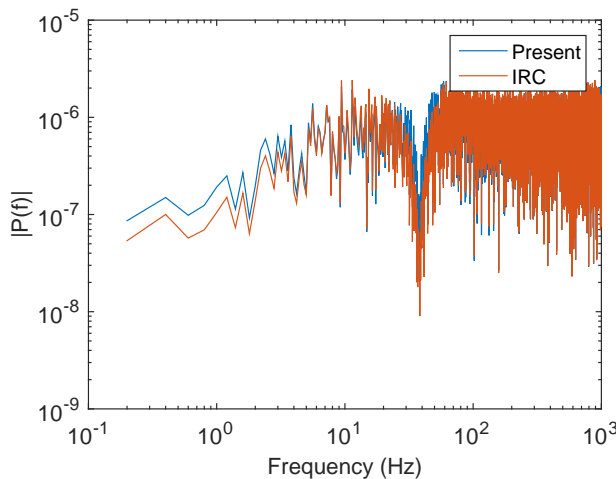


Figure 4.18: Sensitivity function (G_{dy}) of the IRC and the present approach

5

Conclusions and Future work

5.1 Conclusions

5.2 Future work

Bibliography

- [1] Fleming A. J. Aphale S. S. and Moheimani R. Integral control of smart structures with collocated sensors and actuators. *IEEE, Proceedings of the European Control Conference 2007*, pages 2595 – 2602, 2007. Cited on pages 16 and 17.
- [2] Giustiniani A. Butcher M. and Masi A. On the identification of hammerstein systems in the presence of an input hysteretic nonlinearity with nonlocal memory: Piezoelectric actuators – an experimental case study. *Physica B: Condensed Matter*, pages 1—5, 2015. Cited on pages 8 and 9.
- [3] Losito R. Butcher M., Giustiniani A. and Masi A. Controller design and verification for a rotational piezo-based actuator for accurate positioning applications in noisy environments. *Iecon 2015*, 2015. Cited on pages 3, 7, 9, 10, and 11.
- [4] Eleftheriou E. Devasia S. and Moheimani R. A survey of control issues in nanopositioning. *IEEE Transactions on Control Systems Technology*, 15(5): 802—823, 2007. Cited on page 1.
- [5] Eleftheriou E. Devasia S. and Moheimani R. Piezoelectrics in positioning. tutorial on piezotechnology in nanopositioning applications. *Physik Instrumente (PI) GmbH and Co. KG.*, Retreived in January 2008. URL http://www.physikinstrumente.com/en/pdf_extra/2009_PI_Piezo_University_Designing_with_Piezo_Actuators_Tutorial.pdf. Cited on pages 1 and 7.
- [6] N. Elmali H., Olgac. Implementation of sliding mode control with perturbation estimation (smcpe). *IEEE Transactions on control system technology*, 4 (5), 1996. Cited on page 14.
- [7] Ljung L. Glad T. *Reglerteori*. Studentlitteratur AB, second edition, 2003. Cited on page 15.
- [8] Guo-Ying Gu, Li-Min Zhu, and Chun-Yi Su. Integral resonant damping for high-bandwidth control of piezoceramic stack actuators with asymmetric hysteresis nonlinearity. *Mechatronics*, 24(4):367–375, 2014. Cited on page 16.

- [9] Daniele Mirarchi. *Crystal Collimation for LHC*. PhD thesis, High Energy Physics Department, Imperial College London, 3 2015. Cited on page 2.
- [10] Kok K. T. Qingsong X. *Advanced Control of Piezoelectric Micro-/Nanopositioning Systems*. Springer International Publishing, first edition, 2016. Cited on pages 7, 14, and 15.
- [11] Liu X. Sun Y. Ru C. *Nanopositioning Technologies*. Springer International Publishing, first edition, 2016. Cited on page 8.
- [12] Website. The ua9 experiment is investigating how crystals could help to steer particle beams in high-energy colliders, Retreived in January 2016. URL <http://home.cern/about/experiments/ua9>. Cited on page 2.